STED nanoscopy : A novel way to image the pore space of geological materials

Hellmuth, Karl-Heinz

2021-08

Hellmuth , K-H , Sammaljarvi , J , Siitari-Kauppi , M , Robinet , J-C & Sardini , P 2021 , ' STED nanoscopy : A novel way to image the pore space of geological materials ' , Journal of Microscopy , vol. 283 , no. 2 , pp. 151-165 . https://doi.org/10.1111/jmi.13016

http://hdl.handle.net/10138/333464
https://doi.org/10.1111/jmi.13016

Received: 11 December 2020 | Revised: 19 April 2021 | Accepted: 20 April 2021

DOI: 10.1111/jmi.13016

Journal of Microscopy RMS

ORIGINAL ARTICLE

STED nanoscopy – A novel way to image the pore space of geological materials

Karl-Heinz Hellmuth[1] | **Juuso Sammaljärvi**[2] | **Marja Siitari-Kauppi**[2] | **Jean-Charles Robinet**[3] | **Paul Sardini**[4]

[1] Radiation and Nuclear Safety Authority (STUK), Helsinki 00881, Finland

[2] Department of Chemistry, University of Helsinki, Finland

[3] Andra, Chatenay Malabry, France

[4] IC2MP UMR CNRS 7285, HYDRASA, University of Poitiers, Poitiers, France

Correspondence
Juuso Sammaljärvi, Department of Chemistry, University of Helsinki, A.I. Virtasen aukio 1, P.O. Box 55, 00014, Finland.
Email: Juuso.sammaljarvi@helsinki.fi

Summary

STED nanoscopy (Stimulated Emission Depletion). which can resolve details far below the diffraction barrier has been applied hitherto preferentially to life sciences. The method is however also ideal for the investigation of geological matrices containing transparent minerals, an application tested here, to our knowledge, for the first time. The measurements on altered granitic rock and sedimentary clay rock, both containing very fine-grained phases, were conducted successfully. The STED fluorophore was dissolved in C-14-labelled methylmethacrylate (C-14-MMA) monomer which was polymerised within the rock matrix, thereby labelling the pore space in the geomaterials. Double labelling provided by the C-14-labelled MMA enables autoradiography and scanning electron microscopy (SEM), providing necessary complementary information for characterisation and quantification of porosity distributions and mineral and structure identification. Promising perspectives for further investigations of geological matrices by using different fluorophores and the optimisation of measuring procedures or even higher resolution are discussed. The combination of these different methods enlarges the observation scale of porosity from nanometre to centimetre scale.

KEYWORDS

autoradiography, crystalline rock, electron microscopy, porosity, sedimentary rock, STED nanoscopy

1 | INTRODUCTION

The availability of nanoscopy based in Stimulated Emission Depletion (STED) in comparison to other microscopic methods using fluorescence or electrons (SEM) is still limited, although increasing. STED has been developed during the last about 20 years[1–6] and has been applied preferentially to studies in life sciences, including living tissues and cells.[7,8] To date, few investigations of geological samples has been proposed using this novel technique. Although high-resolution electron microscopic methods [scanning electron microscopy (SEM) and transmission electron microscopy (TEM)] are continuously contributing to progress in petrographic research, straight-forward lens-based optical microscopy still has a key role in the investigation of the pore space of rocks and mineral-based matrices.[9] STED microscopy has been implemented with rather different laser systems ranging from femtosecond pulsed to continuous-wave lasers. This shows the variability of the methodology, but this wide range of options

may confuse untrained users looking for simplicity and high-resolution power.[10]

The dimensions of rock pore parameters cover such a wide range that a multitude of characterisation methods has to be applied for the investigation of both bulk and spatial, mineral-specific properties.[11–18] Fracture networks and spatial distribution of porosity can be conveniently characterised – with certain limitations of resolution – by optical microscopy and autoradiography using radioactive tracers and PMMA (polymethylmethacrylate) method.[19–23] In crystalline rocks, fracture networks have been characterised and porosities measured on the scale of mineral grains. However, highly porous regions such as altered and clay phases could not be studied in greater detail due to resolution limitations given by the range of the C-14 beta rays of the C-14-PMMA tracer used (20 μm). The same limitations apply to clay stones in general, but the use of H-3-PMMA brought some resolution improvement, reaching nearly 10 μm.[17,24] Recently the combination of different techniques such as the C-14-PMMA method, X-ray μ-CT and SEM has been proven to be a powerful tool to characterise crystalline rocks in 3D, allowing the creation of a more realistic representation of the rock matrix for reactive transport modelling in heterogeneous matrices.[25–27]

Pioneering work using fluorescence and confocal scanning laser microscopy has been done within the Spanish nuclear waste program[19,20] where microfractographic methods mainly for crystalline rocks were developed. Fluorescence microscopic methods in general offer the advantage of simple sample preparation but provide limited spatial resolution. Advantages and disadvantages of fluorescence microscopic methods include characteristics such as resolution (*xy, z*), temporal resolution, imaging depth, usability, cost, signal/noise ratio and photobleaching.[28] However, the resolution of confocal laser microscopy based on fluorescence is limited by the wavelength of the laser light used to about half of the wavelength, which is not sufficient to study nanometre-scale rock pores.

Fluorescence-based microscopy and nanoscopy depend on the use of fluorescent dyes, for example fluorophores. It was clear that fluorophores, which are common in microscopic petrographic work, might not work for STED. That is because using STED, the revolutionary idea to overcome the diffraction barrier was to use two molecular states of the fluorescent marker and photons switching between these states. Thus the photophysical and photochemical properties of the marker such as fluorescence lifetime, quantum yield, fluorophore stability against bleaching and oxidation, suitable absorption and emission wavelengths, solubility and presence of reactive groups are of outstanding importance. Some of these depend on the technical equipment available, for example on laser sources and filters. For application to geological material, reactive groups were considered not important at this preliminary stage; later, for interaction with minerals or intercalation within sheet structures (clay minerals), for example, charged marker molecules might be beneficial.

In the present paper, a possible application of STED is proposed for visualising and characterising the pore space of rocks with nanometre-scale pores. Such kinds of materials are very common; many different kinds of geological materials such as altered crystalline rocks, sedimentary clay rocks (such as mudstone and shale), or anisotropic cementitious materials contain mainly nanometre-scale pores, which are difficult to resolve using classical optical microscopy or even SEM. The advantage of lens-based microscopy and autoradiography is the ease of use, the 3D capability of the former and the capability to conduct studies on the rock core scale of the latter, as well as the possibility to calibrate the measurement of the emitted radiation for porosity determination. STED has been used to depths of more than 100 μm[29]; it is expected that transparent mineral phases will allow also investigations below the ground rock surface.

The application of STED to geological materials raises the following questions:

1. Is STED easily adaptable from biological samples to crystalline and clay rock samples?
2. Is STED a possible method to characterise pore space of crystalline and clay rock?

Sample preparation methods and suitable dyes, which differ from those used for biological materials, are tested. While in life sciences, biomolecules are marked with a suitable, reactive fluorescent dye, in a geological material, the space is marked by the impregnation with a resin in which the tracers are immobilised. Wide-field UV microscopy was utilised as a supplementary technique for preliminary scoping imaging and selection of suitable geological samples. UV microscopy will also provide a point of comparison to STED nanoscopy. We will also test a double labelling technique, which allows for autoradiography by using a radioactive tracer (C-14-MMA) and STED by using a suitable fluorescent dye (fluorophore), both after mixing in a monomer MMA (methylmethacrylate) solution and fixed by polymerisation. Two different rock types were analysed with STED (crystalline granitic and sedimentary clay rock) because the pore space of these two rock types is very different: granitic rock contains a lot of microcracks and also microporous altered minerals, whereas the porosity of sedimentary clay rock is mainly made of nanometre-scale pores.

2 | MATERIALS AND METHODS

2.1 | Geological samples

Crystalline rock sample was available from the Finnish geological disposal site program for a nuclear waste repository. A rock sample from the Syyry site investigation area, Central Finland (drill core SY1) was selected for this work. As the Finnish crystalline bedrock from the Sievi, Syyry site, generally, is rather fresh or only slightly altered, a large number of drill cores had to be checked to find a more strongly and selectively altered sample, containing highly porous phases with very small pores.[30,31] The main rock type at this site is a slightly foliated, grey tonalite showing locally various degrees of alteration, consisting essentially of quartz, plagioclase and Na-feldspar, usually with biotite and amphibole. It also contains K-feldspar (< 3%), muscovite, epidote, apatite, sphene, chlorite, zircon and opaques as accessory minerals. Alteration features, predominantly found along conducting fractures, were variable degrees of plagioclase seritisation and biotite chloritisation. The sample studied here was SY1, 917 m, which is tonalite with mylonitic disrupture and strongly altered plagioclase partly replaced by sericite. Chloritised biotite has a porosity of 1.0%–3.0%. Fissure fillings of hydrothermal origin (laumontite, analcime, prehnite), weathering products (montmorillonite, kaolinite, calcite) and deformation (quartz, epidote, chlorite) were also found.[31] In sample SY1-917 m highly porous sheared and altered zones dominate where porosities were above 5%. Altered phases in crystalline rock, in general, tend to shift in pore size towards a smaller radius, mostly tens of nanometres compared to microfracture apertures of micrometre scale in unaltered samples.[12,32]

Sedimentary clay rock samples (core number EST26095) were extracted from the French Callovo–Oxfordian mudstone formation (east part of the Paris Basin) investigated in the framework of the French radioactive waste deep geological repository program. The Callovo–Oxfordian mudstone (COX) is fine-grained; on the scale of centimetre–millimetre, the mineral distribution of the rock is relatively uniform without any particular features. Average bulk porosity is about 14%, the connected porosity is mainly located in the clay matrix (illite/smectite clay type), whereas carbonate and tectosilicate grains (quartz, feldspars) are essentially nonporous. Pore size is mainly distributed between 2 and 100 nm.[33] The microporous clay matrix presents an average porosity of 40%−45%. As accessory minerals, pyrite aggregates can be associated with high or low porosity.[34] Porosity maps derived from the H-3-PMMA autoradiography method were compared with SEM-BSE mineral maps.[17] Essentially, at the scale of a pixel of the autoradiograph ($20 \times 20\ \mu m^2$), the measured porosity results from a mixing of microporous clay and nonporous carbonate and tectosilicate, that is difficult to resolve by SEM. In this work, the aim is to compare the C-14-PMMA autoradiographic images to STED images and see if this combination improves the detection of nanometre-scale pores at the scale of the autoradiograph pixel. Mudstone samples are very brittle and easily break upon preparation by drilling or sawing along the bedding planes. The samples here were stabilised by the impregnation with C-14-PMMA allowing us to study centimetre-scale areas without disturbances.

2.2 | Methods

2.2.1 | Fluorescence dye selection for geological material impregnation

In order to perform both STED nanoscopy and autoradiography, a given sample needs to be impregnated with both a radioactive tracer and a suitable fluorophore. The fluorophore selection process was therefore guided by the need to fix the fluorophore in place by a solid resin, and the desire to incorporate double labelling with a radioactive tracer into the impregnation protocol. Therefore, we decided to use MMA as a solvent and work with fluorophores that were, or could be made, soluble in it. This solvent allows for fixation of the fluorophore in place via polymerisation and is employed in the PMMA autoradiography, which can provide quantitative measurement of the spatial distribution of porosity.[21,32,35] By doing the impregnation with a mixture of C-14-MMA and fluorescent colorant, we aim to combine two imaging techniques for studying the pore space at different scales. Thus, the solubility of the colorant in MMA is important. The homogeneous distribution of both tracers in PMMA after polymerisation is important too for preserving the photooptical characteristics also in the solid matrix. For preliminary scoping imaging and selection of suitable geological samples, conventional wide-field fluorescence microscopy was used which was working with photoactivation in the UV at 360 nm (Hg lamp). The properties of the fluorophores studied in this work are summarised in Table 1.

As a first test, we tried to use the Eu(III) complex as a fluorophore for imaging pore space using STED. Wide-field fluorescence micrographs of a generic altered granite impregnated with $Eu(TTA)_3$ $(TBPO)_2$ in PMMA (excitation with 360 nm UV) were done on the first try. The strong fluorescence of Eu(III) should make also small pores visible. A simple synthesis method was applied to create an Eu(III) chelate complex, which improves the light absorption properties of Eu(III) and makes it soluble in MMA. Europium beta-diketones have good luminescent

TABLE 1 Fluorophores studied in this work

Fluorophore	STED/UV	Excitation wavelength max	Emission wavelength max
Eu(TTA)3(TBPO)2	UV	360 nm	612 nm
Lumogen Red F305	STED	578 nm	613 nm

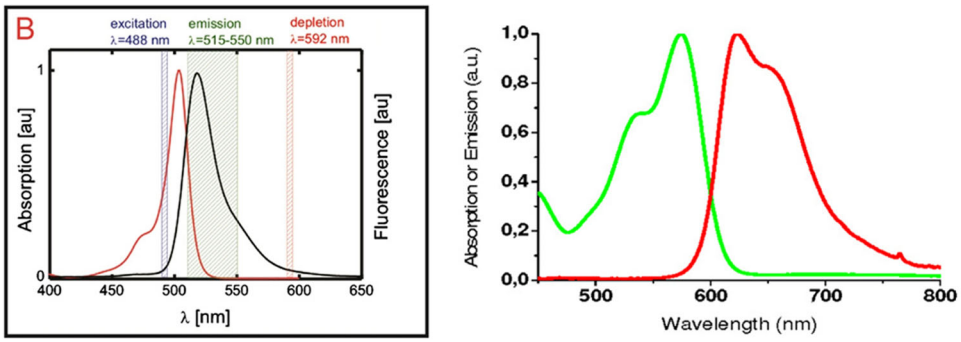

FIGURE 1 Typical absorption and emission spectrum of dye suitable for STED nanoscopy (left); suitable, optimized excitation, emission and STED depletion wavelengths are indicated[5] and absorption and emission spectrum of Lumogen F Red 305.[39] Right-hand side legend: Green line: Excitation spectrum; Red line: Emission spectrum

properties due to the unique electronic structure (f–f transitions) of Eu(III) and the antenna effect of the ligands leading to efficient energy capture and transfer to the metal ion and high fluorescence yield within a narrow emission band.[36,37] The beta-diketone complexes generally contain two molecules of coordinated water which is bound to the central cation according to its geometrical preferences in complexes. The coordinated water can be replaced by neutral electron donors such as phosphine oxides, which increases the solubility of the complexes in organic phases such as MMA.

In solid matrices such as PMMA, the thermal stability of the complexes is enhanced and luminescence concentration quenching is reduced. Eu(III)-β-diketonates and their adducts with e-donors usually emit a hypersensitive, strong red fluorescence (for these types of transitions the term luminescence actually would be more adequate). They are very efficient for wide-field fluorescence microscopy with UV excitation; however, the electronic $^5D_0$-^7F transitions around 612 nm are characterised by very sharp bands and long phosphorescence lifetimes in the milliseconds range.[38] These properties render the positioning of the depletion radiation wavelength for STED difficult and prevent rapid switching. However, they are still useful in complementary UV microscopy.

As further candidates for the marker commercially available compounds of the rhodamine and perylene families were considered. Both have high fluorescence quantum yields, suitable absorption, and emission wavelengths, and photostability and consequently have been used for STED. Perylenes seem to be more photostable due to the central perylene structure resembling graphite, but stacking reduces solubility. Perylene red (e.g. Lumogen Red F305 or F300, BASF) has been designed especially for use in PMMA. Its maximal absorption wavelength is 578 nm (PMMA), maximal emission wavelength is 613 nm (www.fluorophores.org) as shown in Figure 1. The compound has a solubility of 5 g/L in MMA solubility which is increased by side groups inclined to the perylene plane. This marker has emission line with a broad Red-shifted shoulder making adjustment of the depletion wavelength easy.

2.2.2 | Sample impregnation

After the tracer selection was made, the rock sample impregnations were started. A rock sample of altered tonalite, SY1-917-1, was impregnated with C-14-MMA.[21] Rock sample SY1-917-2 were impregnated with single marker labelling using Eu(TTA)3 $(TBPO)_2$. Another tonalite sample (ref. SY1-917-3) was impregnated with single marker labelling using Lumogen Red F305 (BASF, CAS No.: 872005-48-6; mol. weight 1207 g/mol) (kindly provided by A. Böhm from Colorflex GmbH, Mannheim, Germany) mixed with MMA. The dye concentrations in MMA used in impregnations were 10^{-4}, 10^{-5} and 10^{-6} M. Double labelling Lumogen Red by addition of C-14-labeled MMA (3700 Bq/mL) was applied on a Callovo–Oxfordian clay-rich rock sample (ref. COX1). For thermal polymerisation, a radical initiator (AIBN, 250 mg/100 mL) was added.[40]

The rock samples were dried under vacuum at 60 °C for about 1 week and thereafter were saturated with Lumogen Red F305- and ^{14}C-labelled MMA also under vacuum for about 1 week. Thermal polymerisation was achieved

TABLE 2 Sample list and impregnation protocols

Sample code	Rock type	Radioactive tracer	Fluorophore	Fluorophore concentration (M)
SY1-917-1	Altered tonalite	C-14		
SY1-917-2	Altered tonalite	Inactive	Eu(TTA)3 $(TBPO)_2$	
SY1-917-3	Altered tonalite	Inactive	Lumogen Red F305	10^{-4}
SY1-917-3	Altered tonalite	Inactive	Lumogen Red F305	10^{-5}
SY1-917-3	Altered tonalite	Inactive	Lumogen Red F305	10^{-6}
COX1	Callovo-Oxfordian mudstone	C-14	Lumogen Red F305	10^{-4}
COX1	Callovo-Oxfordian mudstone	C-14	Lumogen Red F305	10^{-5}
COX1	Callovo-Oxfordian mudstone	C-14	Lumogen Red F305	10^{-6}

at 58°C within about 24 hours. The impregnated cores were cut by low-speed diamond saw and the surfaces were ground and polished; for autoradiography, grinding with 1000 mesh silicon carbide was sufficient, for STED also polishing with 0.25 μm diamond paste was used for part of the samples. For STED analysis, we prepared thick (2–3 mm) polished samples of the crystalline rocks with or without cover glass and thin sections (thickness about <30 μm) with and without cover glass, dimensions of about 10–15 mm. The use of epoxy resin for fixing the cover glasses didn't always result in fully clear products and air inclusions were sometimes present. All samples were fixed with epoxy resin on standard microscopic slides (76 × 25 mm^2) on the centre part of about 20 × 20 mm^2. The samples SY1-917-3 and the double-labelled samples, COX1, were analysed by STED in the laboratory of Biophysics in Turku, Finland.

The samples and the protocols applied to them are summarised in Table 2.

2.2.3 | C-14-PMMA autoradiography

After the sample preparation, autoradiographic imaging of the C-14-MMA-labelled samples was performed. C-14-PMMA autoradiography is based on measuring the radiation from the sample material impregnated with C-14-labelled methyl methacrylate (C-14-MMA), and imaging its distribution throughout the sample. In this method, the rock is impregnated with low-viscosity MMA doped with C-14 or H-3. After total impregnation of connected pore space, MMA polymerisation and subsequent sample handling and digital image analysis, autoradiography delivers the quantitative porosity map of sample sections.[32,35] The autoradiography employed in this work was based on the storage phosphor screen technique. BAS TR2025 phosphor–europium complex imaging plates were used in this work. The scanner used to read the autoradiography imaging plates in this work was the Fuji FLA-5100.

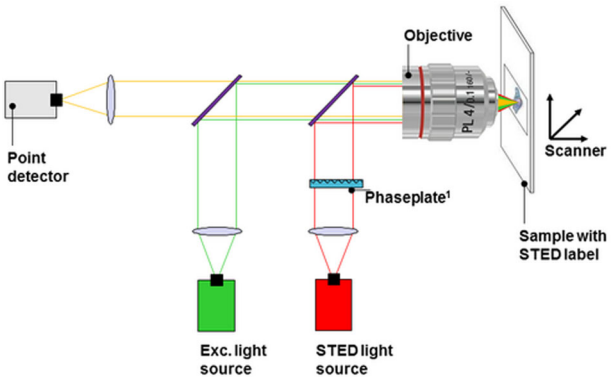

FIGURE 2 Diagram of the design of a STED device. The double laser design allows for excitation and stimulated emission to be used together for STED (from https://www.abberior.com)

2.2.4 | STED nanoscopy analyses

Superresolution microscopy was tested for visualising and characterising the pore space of rocks presenting nanometre-scale pores. Stimulated emission depletion (STED) microscopy is one of the techniques that make up superresolution microscopy. As nanometre-scale features can be distinguished using this technique, it can also be called nanoscopy. STED creates images by the selective deactivation of fluorophores, minimising the area of illumination at the focal point and thus enhancing the achievable resolution for a given system (Figure 2). In this work, we decided to use Lumogen F Red 305 as the fluorophore and it was fixed in place via the impregnation protocol described in Section 2.2.2.

To implement the STED technique, the microscope design needs to include a second light beam (STED light) besides the excitation beam. Molecules in areas subject to STED light above the saturation threshold are forced into the off state.

Here the initially used Leica TCS STED on SP5 platform was one of the first superresolution microscope systems introduced in 2004. It is equipped with four standard

pulsed excitation lasers; there are two lasers for STED excitation (532 nm and 635 nm) and one for depletion (tuneable within 690–1040 nm). The high-aperture microscope objective used was 100×, oil immersion, numerical aperture (NA) 1.4. Later, the next-generation instrument was used, which also combined confocal and STED options (Abberior Instruments GmbH, Göttingen, Germany; the instrument is a resource of the EuroBioImaging organisation). This equipment has three excitation lasers: 488, 561 and 640 nm and two depletion lasers: 580 and 775 nm; it has also 3d STED (special energy distribution) in the axial direction, thus giving an improvement in axial resolution. Both instruments were located at the Laboratory of Biophysics of the University of Turku (Finland).

Surface polished thick samples and thin sections for petrographic investigations are often routinely prepared with cover glass, which is adapted to the refractive index of standard immersion oil. Although covered samples could be investigated with STED, it was found that there is no need for such mounting procedures. At the scales of these images, no clear differences between surface-polished and covered samples were observed. At the limit of resolution, aberrations caused by the different materials between sample surface and lens probably become more decisive. Thin sections which must be as thin as possible (<30 μm is desirable) have the advantage that the laser beam can be easily directed to the desired mineral grains. Thick sections allow the investigation of deeper layers allowing 3D images. When investigating rock samples it is beneficial to avoid possible artefacts of near-surface zones and go further into the depth; in living tissues, depths of more than 120 μm were achieved by STED.[29] To avoid the surface imperfections, most measurements were started already at a certain depth, about 10 or 20 μm; the scanning depth was increased in steps of 0.5 μm. In the images of this work, only one plane of 40 steps is shown.

In rock matrices, transparency is expected to show greater variability, depending also on the orientation of mineral grains. All materials with a different refractive index between lens and sample surface can cause aberrations.[41] The refractive index of standard immersion oil is 1.518; that of PMMA is about 1.489 (depending on the degree of polymerisation) while those of the main mineral components in granitic rock are slightly higher (1.53–1.59).

A general problem with geological samples is the location of the laser beam, while on thin sections the position could be roughly determined, in thick samples incisions cut from the margins served only as a poor aid to find the position. We also tried to use Al foil with punched circular holes of 3 mm diameter, but foil thickness (90 μm) and imperfect flatness of these templates disturbed the free movement of the optical lens. Most manufacturers give a maximum working distance of about 130 μm; Leica gives 90 μm. Experimental platforms allowing the integration of light microscopy and SEM by placing the objective lens into the vacuum chamber of the SEM recently became available. Thereby correlative information within exactly defined regions of interest can be achieved.[42] Such a platform is also commercially available by Delmic company (Delft, The Netherlands) and can be used also for STED–SEM integration. At the STED platform we used we did not have that option. For geological samples, there would be additional testing on sample mounting practices needed.

2.2.5 | Electron microscopy on impregnated samples

The samples prepared for STED nanoscopy were carbon coated for the SEM analyses and the analyses were performed using a field emission scanning electron microscope (FE-SEM). Hitachi S-4800 (Hi-tachi, Tokyo, Japan). model with Oxford instruments X-sight X-ray diffractometer. The energy resolution of the EDS detectors used is about 130 eV for Mn Kα with processing capabilities multichannel analyser with 2048 channels at 10 eV/ch. The FE-SEM-EDS systems were operated by Oxford Instruments INCA and AZtec software. The analytical data obtained was semiquantitative and the sum of the components was normalised to 100%. Typical detection limits in point analysis for different elements range between 0.3 and 0.5 wt%. The FE-SEM-EDS was used in high-vacuum mode with backscattered signal, 20 kV accelerating voltage and 1–5 nA probe current. The backscattered electron (BSE) images and elemental distribution maps were obtained.

3 | RESULTS

Granitic rock

Figure 3 presents the porosity patterns of sample SY1-917-1 determined with C-14-PMMA autoradiography method. A typical feature in autoradiographs of many granitic rocks are zones of enhanced porosity, mostly having the form of mineral grains, which are distributed within a porous network of cracks/fissures. Most frequently, such features are observed in altered/weathered rocks. The crystalline rock sample observed in this work (Sievi tonalite, sample ref. SY1-917) presents strong hydrothermal alteration features. Alteration is visible in the image of the rock section (Figure 3, left) discoloration due to biotite alteration and oxidation of part of the Fe(II). Feldspar grains are milky due to sericite formation. In the autoradiograph, the dark areas indicate high porosity in these altered phases.

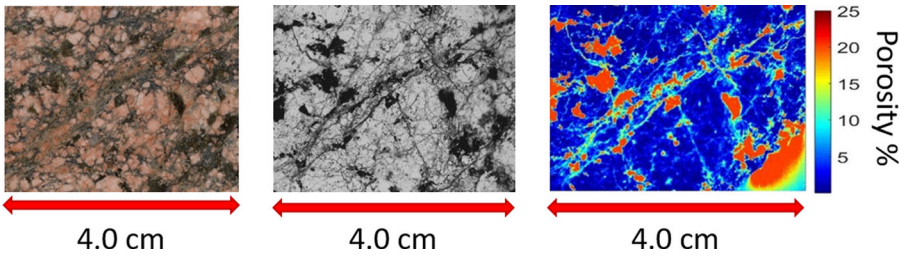

FIGURE 3 Photo image of rock sample SY1-917-1 (left) and the corresponding C-14 PMMA autoradiograph (centre) showing the porosity distribution of the sample. Porosity map from storage phosphor screen autoradiograph (right; down right below corner of the sample is missing in the porosity map). Total porosity of altered tonalite was determined to be 7% ± 1% in this sample; the highest porosity of altered phases is around 20%. The pixel size in these images is 10 μm

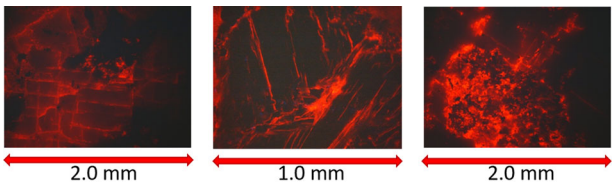

FIGURE 4 Wide-field fluorescence micrographs of altered granite demonstrating different types of porosity (impregnated with $Eu(TTA)_3$ $(TBPO)_2$ in PMMA; excitation with 360 nm UV) showing feldspar (left), magnification 50×, biotite lamellae (centre), magnification: 100× and porous fine-grained altered phases (right), magnification: 50×

In order to improve the visibility of tiny fissures in the matrix, a rather long exposure was used which overexposed the more porous phases. These porous phases are most often sheet silicates (biotite, chlorite, different clay minerals) with a large number of pores having apertures below the resolution limit of the autoradiography, and most optical microscopical methods. Figure 3 (centre) shows the increased intergranular porosity while most details in the mineral grains are not visible. In the albite grain, there are conspicuous leaching features increasing the intragranular porosity. With C-14-PMMA autoradiography, the porosity was determined to be 4%–9% in altered grains; the same values were obtained by image analysis from the BSE images. Pore diameters measured by Hg-porosimetry were in a wide range of 2–50 nm (mesopores) and >50 nm (macropores).[31] Figure 3 (right) also presents a porosity map of the sample. It can be seen that there are several areas with porosity of around 20%. These correspond with highly altered areas containing fine-grained alteration products.

Figure 4 shows wide-field fluorescence micrographs of an altered granite impregnated with $Eu(TTA)_3$ $(TBPO)_2$ in PMMA demonstrating different types of porous phases. In the feldspar (Figure 4, left) fissures perpendicular to the surface are sharp while inclined fissures are blurred by fluorescent light from different depths within the translucent feldspar. This is particularly disturbing in the case when sericite inclusions are present which cause an intense illumination of the whole grain. Also in the somewhat less transparent biotite (Figure 4, centre), lamellae in the centre are only partly clear. The structure of very porous, altered fine-grained phases (Figure 4, right) is not resolved and there are also opaque phases in this region. These regions are not resolved by C-14 PMMA autoradiography either. Suitable rock samples were selected with the help of these two imaging methods for investigation by STED.

SEM BSE imaging of SY1-917-1 is shown in Figure 5. The image on the left shows a highly altered fine-grained, iron-rich phase. Other features present are plagioclase grains, smaller epidote grains and fine-grained chlorite phase. The image on right shows a fissure surrounded by fine-grained alteration products. Plagioclase has experienced seriticisation and amphibole has become fine-grained.

In the confocal/STED images (Figure 6), very sharp fissures are visible in the feldspar. In the altered tonalite, there are features resembling clay minerals which are sharper in the STED imaging compared to confocal imaging. At high magnification, there are significant areas of lower porosity in the rock matrix and finding specific porous regions proved time consuming. In general, in the STED images there are more details visible than what C-14-PMMA autoradiographs or conventional microscopy can reveal. SEM images of these areas could not be prepared, because the exact positions could not be found. Therefore, interpretations concerning the nature of the alteration phases are not possible at this preliminary level of the measurements.

Sedimentary clay rock (mudstone)

Figure 7 presents the distribution of porosity at the scale of the sample using C-14-PMMA method. The sample was impregnated with MMA that was double labelled with Lumogen Red F305 and C-14 beta emitter. Using C-14-PMMA method, total porosity of the COX sample was

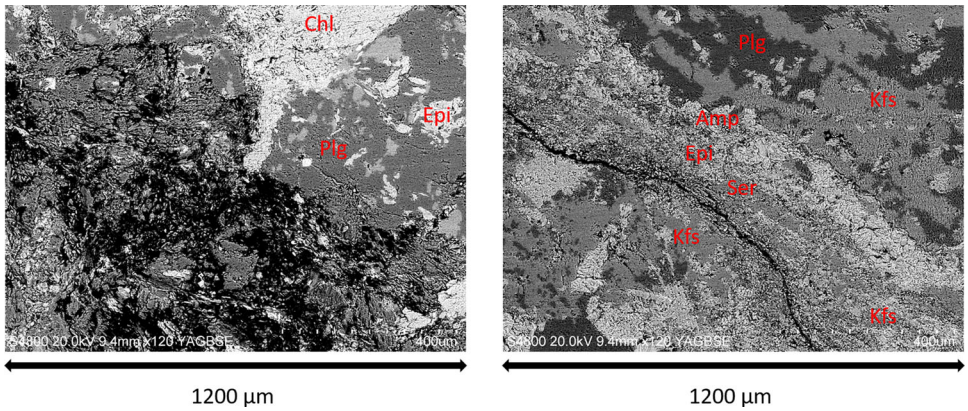

FIGURE 5 SEM BSE imaging of SY1-917-1. Left: Highly porous iron-rich phase. Intact plagioclase and epidote grains. Highly chloritized grain. Right: Fissure surrounded fine-grained sericite and amphibole. Farther from the fissure are unaltered plagioclase and potassium feldspar grains. Legend: Amp = Amphibole; Chl = Chlorite; Epi = Epidote; Kfs = Potassium feldspar; Plg = Plagioclase; Ser = Sericite. The pixel size in these images is 413 nm

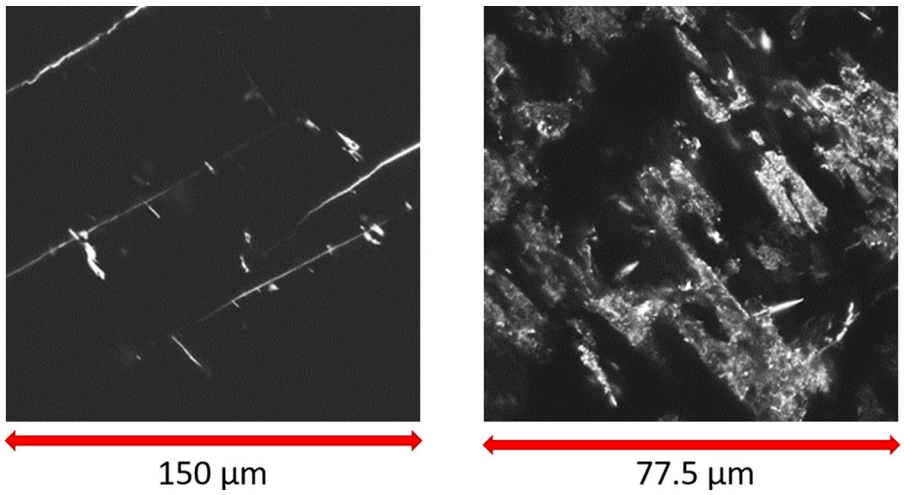

FIGURE 6 Confocal/STED images (one out of up to 40 planes, taken in steps of 0.5 μm) of SY1-917-2 impregnated with Lumogen Red in PMMA showing tiny fissures in feldspar (left). Structures in highly porous altered phases (right). The pixel size in the image on left is 39 nm. The pixel size in the image on right is 19 nm

determined to be 12% ± 2%; this value is in agreement with the porosities previously found by Robinet et al.[17] The rock is very homogeneous in both the rock image and the autoradiograph, as seen Figure 7. The visible cracks are obviously artefacts caused by shrinking during the drying process. In the autoradiograph there are tiny light grey spots representing less porous calcareous phases, appearing in blue (low porosity) in the porosity map.

The detailed porosity at the scale of the pixel of the autoradiograph (20 × 20 μm^2) cannot be resolved by any autoradiographic method, and even the use of SEM (Figure 8) is not sufficient to describe the porosity distribution at this scale, because pores are mostly nanometre size in the clay matrix. SEM imaging however provides mineralogical information, which could be correlated with the STED porosity data. SEM imaging of the COX sample shows that the chief features at the micrometre scale are large (about 10- 100 mm) quartz and carbonate grains, and smaller (about 1–10 mm) framboid-shaped pyrite grains. Besides these larger grains, the bulk of the sample matrix is composed of fine-grained clay minerals.

Figure 9 shows STED images of the COX sample. It represents a general view of the detailed porosity of the COX sample (the bulk content of pyrite is quite low in this clay rich rock; see for instance Figure 8). On the overview seen on the upper left of Figure 9, some round shapes and pyrite framboids are clearly visible surrounded by porous clay ground mass. Conversely, on the overview at the lower left of Figure 9, the nonporous and angular shaped grains correspond to quartz or carbonate. A few holes (white spots)

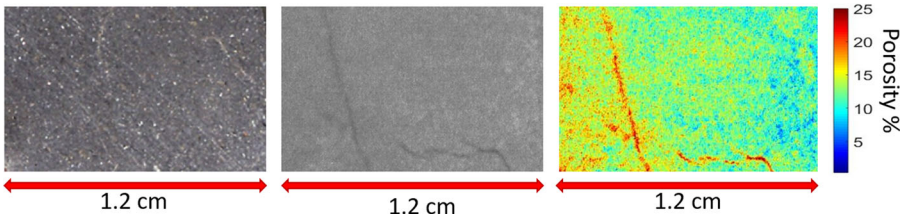

FIGURE 7 Photo image of COX clay rock sample (left), corresponding C-14-PMMA autoradiograph (centre) and porosity map of the sample (right). In autoradiograph, darker the shade higher the porosity. Porosity map was obtained from storage phosphor screen autoradiograph technique. The pixel size in these images is 10 μm

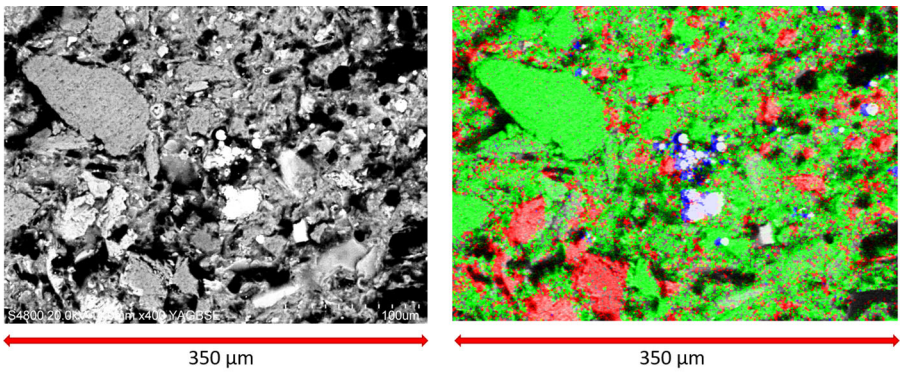

FIGURE 8 BSE image (left) and combination of elemental maps (right) of COX sample showing the spatial distribution of the minerals at the scale of several hundred micrometres. Nonporous quartz grains (in top left there is a 100 μm size quartz grain), nonporous carbonate grains (red), pyrite (blue/white) and clay matrix mass (green) are distinguished by the elemental map combination. Some macropores are individualised at this scale (black colour), but the tiny pores of the clay matrix are not clearly revealed. Pixel size in these images is 124 nm. (Colour legend: Green: Si; Red: Mg; Black: C; Blue/White: S)

are visible on the clay rich area. The detailed views (right of Figure 9) allow discerning the porosity structure of the clay rich zone at the scale of the autoradiograph's pixel. Note that the focal plane of overviews and magnified views images is not exactly the same. The STED images were clearly sharper than the confocal images and a multitude of small-scale features and phases present in the clay mineral groundmass could be observed. The STED images of Figure 9 show that the fluorophore is found practically throughout the whole sample area. Only a few conspicuous grains have very low amount of fluorophore, indicating low porosity. These are pyrite grains; the patterns of these pyrites were used as markers to return to certain regions of interest. They can easily serve also as marker in SEM investigations because as heavy minerals, they are clearly visible, particularly in the BSE mode.

Quartz and carbonate grains appear nonporous at this scale; this is an information that was previously deduced from the combination of autoradiographic and SEM/BSE analysis.[17] STED images here present a direct observation of the spatial distribution of porosity into the specific minerals. Within the clay matrix, the pore geometry is not fully resolved but porosity appears to be evenly distributed. No particular variability was evident at the interface between clay matrix and the largest mineral grains. These findings are relevant in order to predict the mechanical and transport properties of the rock, which depends on clay matrix properties and the content of the nonporous grains.[25,43]

4 | DISCUSSION

Far-field fluorescence nanoscopy is almost ideal for investigating the three-dimensional (3D) interior of transparent matrices, because it can resolve details far below the wavelength of light. This statement is valid up to certain limits also for natural or artificial geological matrices. On STED devices that were previously only used and optimised for biological samples, we performed the first imaging of geological matrices successfully. For the first measuring sessions, a significant number of samples had been prepared from several altered granitic rocks from Finnish disposal site candidates which were impregnated

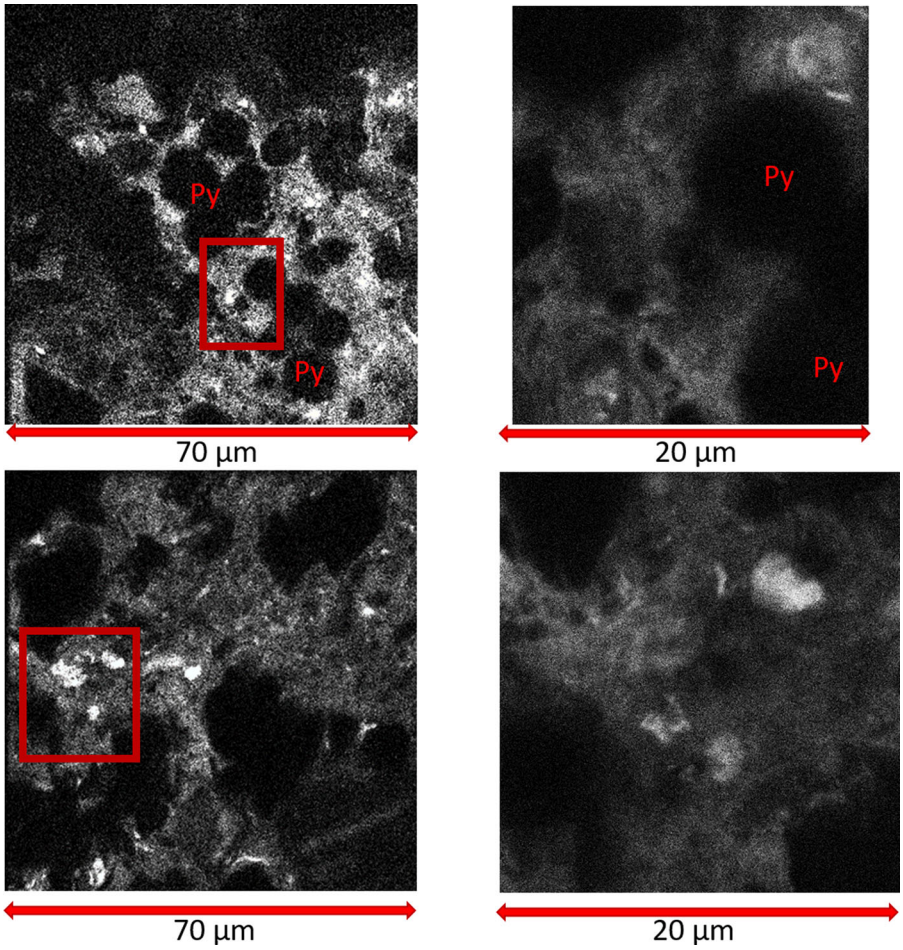

FIGURE 9 Upper left: STED mode image of the COX sample, containing pyrite framboids. Pixel size is 200 nm. Upper right: A detailed view of the upper left picture, where image size is $17.9 \times 20.4\ \mu m^2$, and pixel size is 20 nm. Lower left STED mode image of the COX sample, of a zone containing quartz or carbonate grains embedded in clay. Image size is $68.8 \times 70\ \mu m^2$, and pixel size is 200 nm. Lower right: A detailed view of the lower left picture, where image size is $20.6 \times 21.6\ \mu m^2$, and pixel size is 20 nm. The rectangles in the left-hand side images represent the regions of interest (ROI) magnified by STED in right-hand side images. Ground porous matrix is mainly composed of clay (interstratified illite/smectite), but contains also small nonporous grains and macropores. In these image, porous zones (zones containing Lumogen dye) appears in white showing the porous phases in the sample. This is the opposite for autoradiographs where in the image dark areas are congruent with the porous phases

with three different concentrations of the fluorophore in MMA and prepared in different ways, surface polished and with cover glass, as thick and thin sections. A large number of images were obtained from all these specimens. Despite the great heterogeneity of the products of the complex alteration processes which have affected these rocks, satisfactory results were obtained for all dye concentrations and surface treatments. All of the dye concentrations provided sufficient contrast for microscopic imaging. A wider set of concentrations could be used in future to optimise the dye concentration. On thick sections, the position of the altered porous phases could not be well adjusted for imaging, while on translucent thin sections, the position of the laser could be more easily observed through an ocular. Due to same reasons, SEM investigations of exactly the same regions of interest were not feasible. A device where both methods are integrated would therefore be ideal. The results for the clay rock could be more easily obtained, because clay phases are nearly evenly distributed in the whole rock matrix and the COX samples are more homogeneous on the drill core scale than the altered granites. Patterns of frequent, nonporous pyrite framboids could be used for orientation purposes in STED and SEM. In the STED images, porosity features were imaged which were not visible by SEM; that was one of the goals of this study. A general problem with geological samples is the location of the laser beam; while on thin sections the position can be easily determined, in thick samples, incisions from the margins gave only a very rough idea of the position. We tried to use Al foil with punched circular holes of 3 mm diameter, but the foil thickness (90 μm) and the imperfect flatness of these templates disturbed the free movement

of the optical lens. Most manufacturers give a maximum working distance of about 130 μm; Leica gives 90 μm.

Sophisticated optimisation procedures of the STED equipment would be necessary to quantify the influences of different fluorophore and sample parameters. Laborious preparations and adjustments of lasers and filters are difficult under conditions where the STED device is not available on site. Optimisation is essential when approaching the limits of resolution. For example, the resolution shows a strong sensitivity to the image signal-to-noise ratio.[44] In geological materials, interaction of the fluorophore with, for example, charges of mineral surfaces can be beneficial when intercalation into very narrow pores for example in sheet silicates is intended. Then the molecular shape, conformation and charge and the solvation of the fluorophore are essential. Theoretically, all nanoscopy techniques provide molecular spatial resolution, which for geological matrices means that single dye molecules intercalated between clay layers could be excited separately if all interferences could be excluded.

The Eu(III) chelate proved to be very useful for selection of suitable rock types by conventional wide-field fluorescence microscopy with UV excitation. However, the use of the Eu(III) chelate as fluorescent marker for STED was postponed here, because no suitable laser wavelength for photoactivation was available on the equipment used. Other issues are the very narrow emission line at 615 nm, which would have needed tests with very precise adjustment of the filter for the depletion laser and the relatively long lifetime of the Eu(III) fluorescence, which would need reconsideration of the whole physical process and the pulsing of the lasers. The ligand TTA is very effectively sensitising the fluorescence of Eu(III),[37] but it was found that the ligand is not very stable during storage in contact with air and sunlight at ambient temperature. The stability of complexes with other more suitable ligands should be studied before considering application to STED. Other Eu(III) complexes with high quantum yields in PMMA were studied, for example, by Moudam et al.[45]

Some Rhodamine dyes and in particular dyes having a perylene central structural unit are stable and sufficiently soluble in MMA. Rhodamine 800 is a plane molecule having a positive charge at the tertiary ammonium group; interactions with negatively charged surfaces of silicates as well as intercalation in interlamellar pores in clays may be possible. Testing would need specific sheet silicates, preferably pure phases or single crystals. In the PMMA polymer matrix, perylene red is more photostable than rhodamine 800.[46] Lumogen Red F305 was used here, but rhodamine 800 was considered for future experiments, because it has a positive charge at the N-atom, which would offer the possibility to study interaction with negatively charged mineral surfaces in sheet silicates. The solubility of the rhodamine ion pairs would need experiments with more hydrophilic MMA-HEMA copolymers.[47–49] Another approach would be to use a polymerisable fluorophore[50] or make a fluorophore polymerisable via a chemical reaction.[51] The preparation of samples of pure biotite, chlorite and vermiculite was attempted, but the low adhesion between the sheets caused problems resulting in sample preparation artefacts and these tests were postponed to the future. Perylene structures are planar, resembling the graphite structure; overlapping of the π-electrons of the aromatic rings decreases solubility in all solvents. Suitable substitution by side groups, which are turned slightly out of the perylene plane increases the solubility of the dyes.[52] The Lumogen dye is a relatively large molecule, but the nearly plane structure might facilitate intercalation in narrow plane pores. The Lumogen Red F 305 molecule has been designed especially for use in PMMA; the solubility in MMA is 0.5 g/L which was found to be more than sufficient even in very-low-porous granites. The dye is particularly photostable and photophysically suitable for STED.

Double labelling is convenient and not prevented by interactions during the polymerisation, so that the benefits of getting information in different scales and with different resolution are achieved. In future, investigations on the dye concentration should be optimised for matrices of different porosity and structure. Regions of porous, altered mineral phases are often oversaturated in autoradiographs where the characterisation of the whole porosity distribution, which is generally dominated by fissures, cracks and grain boundaries, is intended. Sometimes the oversaturation of the photon detectors was observed in the confocal/STED measurements, but that could depend on the type of detectors used. Obviously, there are extreme differences in fluorescence emission in these regions. These are primarily caused by the amount of dye (porosity) in these phases, but also the transparency of certain phases to light must be assessed. Generally, a complex structure of porous regions not resolved by C-14-PMMA autoradiography was observable qualitatively. Use of the quantity of the emitted fluorescent light to make quantitative estimates concerning porosity seem to be difficult due to photophysical reasons (absorption and scattering), but half-quantitative estimations might be possible. A higher resolution PMMA autoradiography by applying tritium as tracer, has been used by Robinet[34] to characterise the clay rock matrix in greater detail than possible using C-14 as a tracer. As explained above, combination with SEM mineral and porosity maps could be used to separate low-porous carbonaceous zones and regions of higher porosity in an argillaceous ground mass (porosity increased from <5% to >30%).[17] However, even at longer exposure times in these phases no details are resolved using the H-3-PMMA autoradiography method.

There were numerous different relict structures in altered phases visible by fluorescence, for example, of grains aligned in preferential directions and also regular patterns, which seem to be connected to microscopically visible regions/grains of varying yellow–green–brown colour, probably indicating different degrees of alteration. These features are as small as about 0.5–1 μm and cannot be resolved by C-14-PMMA imaging. In the crystalline rock SY1-917 m such features are abundant; they could not be studied in greater detail in these preliminary method tests.

Similar features as those observed here by STED have been reported in work on pseudomorphic alteration (microscopic, SEM, BSE and TEM images); clay minerals are also known to occur as pseudomorphs. The study of those phenomena is a potential application for STED and might even in part replace TEM which needs more sophisticated sample preparation and operation, if sufficiently high resolution could be achieved. There are numerous examples in which, even with high levels of alteration, the morphological features of, for example, original plagioclase crystals are preserved in various sheet silicates. It was also observed that smectite can be formed inside plagioclase crystals, and probably originates from inclusions of muscovite contained in these crystals.[53] Fresh and weathered biotite is often present in soils, which form on slopes from bedrock, and is then found as individual minerals or in rock fragments. In many cases pseudomorphs, formed by a variety of secondary minerals are found to occur between the lamellae. There were secondary minerals, which retained some of the original biotite structure, for example vermiculite and smectite. Micromorphological aspects of biotite weathering are discussed and illustrated in detail in Bisdom et al.[54] In situ weathering products from granitoid rocks of NW Portugal were studied by Sequeira Braga et al.[55]; the resulting saprolites are characterised by the preservation of the original granitic structure and texture. The principal mechanism responsible for the weathering of primary minerals is the transformation of mica into sheet silicates. Detailed complementary SEM and XRDF studies would be needed to shed light on these important weathering mechanisms relevant in soil science as well as for understanding radionuclide retardation.

Proceeding to smaller pore apertures would need more investigations, possibly including different types of model matrices. The ideal would be initially to study small pores, which are ordered and aligned as in pseudomorphic altered phases confined in a rigid granite matrix and having sufficient distance from each other. For that purpose, some of the altered rock types used here seem to be superior to preparations of bulk clay phases where orientation of the clay phases is mostly random. The advantage of the impregnation with double-labelled PMMA (fluorophore and C-14 or H-3) is the fixation of the mineral structures, even if they, in case of clay, may be affected by the structure or charge of the dye molecule itself.

STED high-resolution fluorescence microscopy might be beneficial to support recent developments of grain-scale matrix transport modelling by confirming model assumptions and giving direct input data. Indeed, the use of pore-scale direct numerical modelling of flow and reactive transport needs an accurate description of microscale rock matrix properties, in particular, of intra- and intergranular pore surfaces, which is limited by the resolution of current X-ray microcomputed tomography (X-ray μ-CT) presently to a scale of about 10 μm.[56,57]

The potential application of STED nanoscopy could be the visualisation of nanometre size porous networks in finely divided materials, such as clays or cementitious materials. Obtaining an adequate polishing state of the planar surface of such materials represents an obstacle for the visualisation of the pores on the observation surface. Using STED's 3D capabilities, a set of 2D slices is obtained, in which the porosity distribution is not influenced by the surface state of the sample. Due to the high proportion of infra 20–50 nm pores in such materials, the geometry of the pore cannot be fully resolved by STED. However, STED images can shed new light on the organisation of the porosity in the composite matrix and at the interface between the matrix and the large minerals. This type of information is essential for the development of a micro-macro model for predicting the behaviour of such materials.

5 | CONCLUSIONS

The starting motivation for this work was to find out whether STED is easily adaptable from biological samples to crystalline and clay rock samples, and if STED is a suitable method for characterisation of the pore space of crystalline and clay rock. The results presented here prove that STED is both easily adaptable to geological samples and that STED is suitable for pore space characterisation of geological materials. To date, this contribution constitutes the first application of STED nanoscopy to visualise nanoporous structures in geological materials. The present work proves that Lumogen Red F 305 dye dissolved in MMA is suitable for STED imaging of these materials. The Eu(III) chelate was also found to be very useful for the selection of suitable rock types by conventional wide-field fluorescence microscopy with UV excitation. The Lumogen Red F 305 molecule proved to be sufficiently soluble in MMA to produce a good level of contrast even in very low porous granites. Satisfactory STED imaging results were obtained for all used dye concentrations, thin and thick sections, and surface treatments. The position of the laser

could be more easily observed on translucent thin sections while this was found to be difficult in thick sections. Some problems arose in SEM investigation of the same regions of interest in granites in the case of thick sections. A device where STED and SEM methods are integrated would therefore be ideal.

The visualisation of pore space at nanometre scale was achieved successfully in a granitic rock and a sedimentary clay rock. In the STED images, porosity features were imaged which were not readily distinguishable by SEM. The granitic rock sample exhibited heterogeneous microstructure with features in centimetre to nanometre scales. The clay rock sample exhibited microstructure where the features are mostly microstructure scale and smaller. The nanoporous features in the clay rock were imaged together with patterns of frequent, nonporous pyrite framboids that could be used for orientation purposes in both STED and SEM. In both of these rock types, nanoscale and micrometre-scale porous features could be distinguished and correlated with mineralogical features on the same length scales. This is a considerable improvement over the common situation where porosity data and mineralogical data are available only on different length scales, or only bulk data is available. The features on all length scales were successfully studied without the necessity of destructive methods for studying nanometre-scale features.

Our work here proved that combining STED to C-14 or H-3-PMMA autoradiography method by double labelling the PMMA resin (fluorophore + radioactive tracer) and SEM allows imaging the pore space of a given rock section, from centimetre to nanometre scales. Combining STED and autoradiography with SEM imaging also gave information on the local mineralogical composition, allowing mineralogical data and porosity data to be correlated on the same length scale. The application of these complementary techniques is well adapted to characterising the porosity evolution of both crystalline rock and finely divided materials, such as sedimentary clay rocks. Other finely divided materials, such as cementitious materials, could be a potential future application.

Another potential application for STED could be the study of pseudomorphic alteration phenomena, which produce clay minerals. Here STED might even partially replace TEM, which needs more sophisticated sample preparation and operation. Detailed complementary SEM and XRDF studies would be needed to shed light on these important weathering mechanisms relevant in soil science as well as for understanding radionuclide retardation.

In the future, sophisticated optimisation procedures of the STED equipment would still be necessary to quantify the influences of different fluorophore and sample parameters. Some optimisations of the method are needed, particularly when studying heterogeneous rock matrices presenting minerals with various optical properties. Optimisation is essential when approaching the limits of resolution, but is difficult under conditions where the STED device is not available on site. The use of the Eu(III) chelate as a fluorescent marker for STED could be another avenue of study if a suitable laser wavelength for photoactivation is available on the equipment used. In geological materials, the interaction of the fluorophore with, for example, charges of mineral surfaces can be beneficial when intercalation into very narrow pores for example in sheet silicates is intended. Then the molecular shape, conformation, charge and solvation of the fluorophore are essential parameters. Some Rhodamine dyes with a positive charge should be considered, because interactions with negatively charged surfaces of silicates as well as intercalation in interlamellar pores in clays may be possible. Proceeding to smaller pore apertures would need more investigations, possibly including different types of model matrices.

ACKNOWLEDGEMENTS

The initial phase of the work has been conducted within the European POSINAM project (FP-people-IAPP 2008, project no. 230635; 10/2009-10/2013). during the stay of the first author at the Lab. Hydrasa at the University of Poitiers in 2011, which is particularly appreciated. Thanks are due for giving thorough theoretical and practical guidance to the STED method (in part at the site) to Lars Kastrup (Dept. of Nanobiophysics, Max Planck Institute for Biophysical Chemistry, Göttingen). with whom also sample preparation and fluorophore selection issues were discussed. He conducted first tests with granites at the STED laboratory setup at the MPI. All measurements in Finland were conducted at the Laboratory of Biophysics, University of Turku under guidance and by Sami Koho, Elena Tcarenkova and Elnaz Fazeli, whose advice and sharing of knowledge is greatly appreciated.

ORCID

Juuso Sammaljärvi https://orcid.org/0000-0003-4254-3161

REFERENCES

1. Hell, S. W., & Wichmann, J. (1994). Breaking the diffraction resolution limit by stimulated emission: Stimulated-emission-depletion fluorescence microscopy. *Optics Letters*, *19*, 780–782.
2. Hell, S. W., & Kroug, M. (1995). Ground-state-depletion fluorscence microscopy: A concept for breaking the diffraction resolution limit. *Applied Physics B, Lasers and Optics*, *60*, 495–497.
3. Hell, S. W. (2003). Toward fluorescence nanoscopy. *Nature Biotechnology*, *21*, 1347–1355.
4. Hell, S. W. (2004). Strategy for far-field optical imaging and writing without diffraction limit. *Physics Letters A*, *326*, 140–145.

5. Harke, B., Keller, J., Ullal, C. K., Westphal, V., Schönle, A., & Hell, S. W. (2008). Resolution scaling in STED microscopy. *Optics Express*, *16*, 4154–4162.
6. Hell, S. W. (2010). Far-field optical nanoscopy. In A. Gräslund, R. Rigler, & J. Widegren (Eds.), *Single molecule spectroscopy in chemistry, physics and biology* (pp. 365–398). Berlin, Heidelberg: Springer.
7. Wurm, C. A., Kolmakov, K., Göttfert, F., Ta, H., Bossi, M., Schill, H., … Hell, S. W. (2012). Novel red fluorophores with superior performance in STED microscopy. *Optical Nanoscopy*, *1*, 7.
8. Busko, D., Baluschev, S., Crespy, D., Turshatov, A., & Landfester, K. (2012). New possibilities for materials science with STED microscopy. *Micron*, *43* (5), 583–588. https://doi.org/10.1016/j.micron.2011.10.003.
9. Anovitz, L. M., & Cole, D. R. (2015). Characterization and analysis of porosity and pore structures. *Reviews in Mineralogy and Geochemistry*, *80*, 61–164.
10. Göttfert, F., Wurm, C., Mueller, V., Berning, S., Cordes, V., Honigmann, A., & Hell, S. (2013). Coaligned dual-channel STED Nanoscopy and molecular diffusion analysis at 20 nm resolution. *Biophysical Journal*, *105*, L01-L03.
11. Sardini, P., El Albani, A., Pret, D., Gaboreau, S., Siitari-Kauppi, M., & Beaufort, D. (2009). Mapping and quantifying the clay aggregate microporosity in medium- to coarse-grained sandstones using the 14C-PMMA method. *Journal of Sedimentary Research*, *79*, 584–592.
12. Hellmuth, K. -H., Klobes, P., Meyer, K., Röhl-Kuhn, B., Siitari-Kauppi, M., Hartikainen, J., Hartikainen, K., & Timonen, J. (1995). Matrix retardation studies: Size and structure of the accessible pore space in fresh and altered rock. *Zeitschrift Für Geologische Wissenschaften*, *23*, 691–706.
13. Fernández-Merayo, N., Siitari-Kauppi, M., Montoto, M., & Hellmuth, K. -H. (1996). Characterization of rock matrix structure using microscopy and 14C-PMMA method for the study of retardation mechanisms in granite. *Radiochimica Acta*, *74*, 211–216.
14. Klobes, P., Riesemeier, H., Meyer, K., Goebbels, J., & Hellmuth, K. -H. (1997). Rock porosity determination by combination of X-ray computerized tomography with mercury porosimetry. *Fresenius Journal of Analytical Chemistry*, *357*, 543–547.
15. Siitari-Kauppi, M., Flitsiyan, E. S., Klobes, P., Meyer, K., & Hellmuth, K.-H. (1997). Progress in physical rock matrix characterization: Structure of the pore space. *MRS Online Proceedings Library*, *506*, 671–678.
16. Durand, A., Wiesner, T., Gardner, M., Robitaille, L., Bilodeau, A., Gagné, C., De Konick, P., & Lavoie-Cardinal, F. (2018). A machine learning approach for online automated optimization of super-resolution optical microscopy. *Nature Communications*, *9*, 5247.
17. Robinet, J. C., Sardini, P., Siitari-Kauppi, M., Prêt, D., & Yven, B. (2015). Upscaling the porosity of the Callovo-Oxfordian mudstone from the pore scale to the formation scale; insights from the 3H-PMMA autoradiography technique and SEM BSE imaging. *Sedimentary Geology*, *321*, 1–10.
18. Hemes, S., Desbois, G., Urai, J. L., Schröppel, B., & Schwarz, J. (2015). Multi-scale characterization of porosity in Boom Clay (HADES-level, Mol, Belgium) using a combination of X-ray μ-CT, 2D BIB-SEM and FIB-SEM tomography. *Microporous and Mesoporous Materials*, *208*, 1–20.
19. Montoto, M., Martínez-Nistal, A., Rodríguez-Rey, A., Fernández-Merayo, N., & Soriano, P. (1995). Microfractography of granitic rocks under confocal scanning laser microscopy. *Journal of Microscopy*, *177*, 138–149.
20. Montoto, M. (2003). Petrophysics at the rock matrix scale: Hydraulic properties and petrographic interpretation. M1: Enresa Report–11/2003.
21. Hellmuth, K.-H., Siitari-Kauppi, M., & Lindberg, A. (1993). Study of porosity and migration pathways in crystalline rock by impregnation with 14C-polymethylmethacrylate. *Journal of Contaminant Hydrology*, *13*, 403–418.
22. Hellmuth, K.-H., Lukkarinen, S., & Siitari-Kauppi, M. (1994). Rock matrix studies with carbon-14 poly methyl-methacrylate (PMMA): Method development and applications. Isotopenpraxis. *Isotopes in Environmental and Health Studies*, *30*, 47–60.
23. Sardini, P., Siitari-Kauppi, M., Beaufort, D., & Hellmuth, K.-H. (2006). On the connected porosity of mineral aggregates in crystalline rocks. *The American Mineralogist*, *91*, 1069–1080.
24. Sammartino, S., Siitari-Kauppi, M., Meunier, A., Sardini, P., Bouchet, A., & Tevissen, E. (2002). An imaging method for the porosity of sedimentary rocks: Adjustment of the PMMA method: Example of a characterization of a calcareous shale. *Journal of Sedimentary Research*, *72*, 937–943.
25. Robinet, J.-C., Sardini, P., Coelho, D., Parneix, J., Prêt, D., Sammartino, S., … Altmann, S. (2012). Effects of mineral distribution at mesoscopic scale on solute diffusion in a clay-rich rock: Example of the Callovo-Oxfordian mudstone (Bure, France). *Water Resources Research*, *48*, W05554.
26. Mazurier, A., Sardini, P., Rossi, A. M., Graham, R. C., Hellmuth, K.-H., Parneix, J.-C., … Caner, L. (2016). Development of a fracture network in crystalline rocks during weathering: Study of Bishop Creek chronosequence using X-ray computed tomography and 14 C-PMMA impregnation method. *Geological Society of America Bulletin*, *128*, 1423–1438.
27. Voutilainen, M., Miettinen, A., Sardini, P., Parkkonen, J., Sammaljärvi, J., Gylling, B., … Siitari-Kauppi, M. (2019). Characterization of spatial porosity and mineral distribution of crystalline rock using X-ray micro computed tomography, C-14-PMMA autoradiography and scanning electron microscopy. *Applied Geochemistry*, *101*, 50–61.
28. Combs, C. A., & Shroff, H. (2017). Fluorescence microscopy: A concise guide to current imaging methods. *Current Protocols in Neuroscience*, *79*, 2.1.1-2.1.25.
29. Urban, N., Willig, K., Hell, S., & Nägerl, U. (2011). STED Nanoscopy of actin dynamics in synapses deep inside living brain slices. *Biophysical Journal*, *101*, 1277–1284.
30. Hellmuth, K.–H., Siitari-Kauppi, M., & Lindberg, A. (1991). Applications of the Carbon-14-Polymethylmethacrylate (PMMA). Impregnation method in studies on porosity and matrix diffusion. *MRS Proceedings*, *257*, 649–656.
31. Siitari-Kauppi, M., Lindberg, A., Hellmuth, K.-H., Timonen, J., Väätäinen, K., Hartikainen, J., & Hartikainen, K. (1997). The effect of microscale pore structure on matrix diffusion – A site-specific study on tonalite. *Journal of Contaminant Hydrology*, *26*, 147–158.
32. Sammaljärvi, J., Lindberg, A., Voutilainen, M., Ikonen, J., Siitari-Kauppi, M., Pitkänen, P., & Koskinen, L. (2017). Multi-scale

study of the mineral porosity of veined gneiss and pegmatitic granite from Olkiluoto, Western Finland. *Journal of Radioanalytical and Nuclear Chemistry*, *314*, 1557–1575.
33. Sammartino, S., Bouchet, A., Prêt, D., Parneix, J.-C., & Tevissen, E. (2003). Spatial distribution of porosity and minerals in clay rocks from the Callovo-Oxfordian formation (Meuse/Haute-Marne, Eastern France) – Implications on ionic species diffusion and rock sorption capability. *Applied Clay Science*, *23*, 157–166.
34. Robinet, J.-C. (2008). *Mineralogy, porosite et diffusion des solutes dans l'argilite du Callovo-Oxfordian de Bure (Meuse/Haute-Marne, France). de l'echelle centrimetrique a micrometrique*. University of Poitiers.
35. Siitari-Kauppi, M. (2002). *Development of 14C-polymethylmethacrylate method for the characterisation of low porosity media: Application to rocks in geological barriers of nuclear waste storage*. Report Series in Radiochemistry. *17/2002* Helsinki: University of Helsinki. https://researchportal.helsinki.fi/en/publications/development-of-c-polymethylmethacrylate-method-for-the-characteri.
36. Guan, J., Chen, B., Sun, Y., Liang, H., & Zhang, Q. (2005). Effects of synergetic ligands on the thermal and radiative properties of Eu(TTA). 3 nL-doped poly(methyl methacrylate). *Journal of Non-Crystalline Solids*, *351*, 849–855.
37. Yan, B. (2017). *Photofunctional rare earth hybrid materials*. Singapore: Springer.
38. Binnemans, K. (2005). Rare-earth beta-diketonates. In K.A. Schneider, J.-.G. Bünzli, & V.K. Pecharsky (Eds.), *Handbook on the physics and chemistry of rare earths* (pp. 107–272). *35* Amsterdam: Elsevier. https://doi.org/10.1016/S0168-1273(05)35003-3.
39. Würth, C., Würth, C., Hoffmann, K., Hoffmann, K., Behnke, T., Behnke, T., … Resch-Genger, U. (2011). Polymer-and glass-based fluorescence standards for the Near Infrared (NIR). Spectral Region. *Journal of Fluorescence*, *21*, 953–961.
40. Sammaljärvi, J., Shroff Rama, M., Ikonen, J., Muuri, E., Hellmuth, K.-H., & Siitari-Kauppi, M. (2016). Free radical polymerisation of methacrylates with thermal initiator in clay rock. *Engineering Geology*, *210*, 70–83.
41. Hell, S., Reiner, G., Cremer, C., & Stelzer, E. H. K. (1993). Aberrations in confocal fluorescence microscopy induced by mismatches in refractive index. *Journal of Microscopy (Oxford)*, *169*, 391–405.
42. Zonnevylle, A. C., Tol, R. F. C., Liv, N., Narvaez, A. C., Effting, A. P. J., Kruit, P., & Hoogenboom, J. P. (2013). Integration of a high-NA light microscope in a scanning electron microscope. *Journal of Microscopy*, *252*, 58–70.
43. Shen, W. Q., Shao, J. F., Kondo, D., & Gatmiri, B. (2012). A micro–macro model for clayey rocks with a plastic compressible porous matrix. *International Journal of Plasticity*, *36*, 64–85.
44. Tortarolo, G., Castello, M., Diaspro, A., Koho, S., & Vicidomini, G. (2018). Evaluating image resolution in stimulated emission depletion microscopy. *Optica*, *5*, 32.
45. Moudam, O., Rowan, B. C., Alamiry, M., Richardson, P., Richards, B. S., Jones, A. C., & Robertson, N. (2009). Europium complexes with high total photoluminescence quantum yields in solution and in PMMA. *Chemical Communications*, 2009, 6649–6651.
46. García-Moreno, I., Costela, A., Pintado-Sierra, M., Martín, V., & Sastre, R. (2009). Enhanced laser action of Perylene-red doped polymeric materials. *Optics Express*, *17*, 12777–12784.
47. Amat-Guerri, F., Costela, A., Figuera, J. M., Florido, F., Garcia-Moreno, I., & Sastre, R. (1995). Laser action from a rhodamine 640-doped copolymer of 2-hydroxyethyl methacrylate and methyl methacrylate. *Optics Communications*, *114*, 442–446.
48. Costela, A., Garcia-Moreno, I., Figuera, J. M., Amat-Guerri, F., & Sastre, R. (1996). Solid-state dye lasers based on polymers incorporating covalently bonded modified rhodamine 6G. *Applied Physics Letters*, *68*, 593–595.
49. Ghanadzadeh, A., Sariri, R., Ghanadzadeh, H., & Zakerhamidi, M. S. (2005). Effect of poly-HEMA hydrophilic gel environment on the photo-physical behavior of rhodamine dyes. *Spectrochimica Acta. Part A, Molecular and Biomolecular Spectroscopy*, *61*, 659–663.
50. Breul, A. M., Hager, M. D., & Schubert, U. S. (2013). Fluorescent monomers as building blocks for dye labeled polymers: Synthesis and application in energy conversion, biolabeling and sensors. *Chemical Society Reviews*, *42*, 5366–547.
51. Ozay, H., & Ozay, O. (2013). Rhodamine based reusable and colorimetric naked-eye hydrogel sensors for Fe3+ ion. *Chemical Engineering Journal*, *232*, 364–371.
52. Neuteboom, E. E. (2004). *Photoinduced processes of functionalized perylene bisimides*. Technische Universiteit Eindhoven.
53. Taboada, T., & Garcıá, C. (1999). Pseudomorphic transformation of plagioclases during the weathering of granitic rocks in Galicia (NW Spain). *Catena (Giessen)*, *35*, 291–302.
54. Bisdom, E. B. A., Stoops, G., Delvigne, J., Curmi, P., & Altemüller, H. J. (1982). Micromorphology of weathering biotite and its secondary products. *Pedologie*, *32*(2), 225–252.
55. Sequeira Braga, M. A., Paquet, H., & Begonha, A. (2002). Weathering of granites in a temperate climate (NW Portugal): Granitic saprolites and arenization. *Catena (Giessen)*, *49*, 41–56.
56. Svensson, U., Trinchero, P., Ferry, M., Voutilainen, M., Gylling, B., & Selroos, J. (2019). Grains, grids and mineral surfaces: Approaches to grain-scale matrix modeling based on X-ray micro-computed tomography data. *SN Applied Sciences*, *1*, 1–16.
57. Svensson, U., Voutilainen, M., Muuri, E., Ferry, M., & Gylling, B. (2019). Modelling transport of reactive tracers in a heterogeneous crystalline rock matrix. *Journal of Contaminant Hydrology*, *227*, 103552.

How to cite this article: Hellmuth K-H, Sammaljärvi J, Siitari-Kauppi M, Robinet J-C, Sardini P. STED nanoscopy – A novel way to image the pore space of geological materials. *Journal of Microscopy*. 2021;*283*:151–165. https://doi.org/10.1111/jmi.13016